One-dimensional Electromagnetic Particle Code: KEMPO1
A Tutorial on Microphysics in Space Plasmas

Yoshiharu Omura

Research Institute for Sustainable Humanosphere, Kyoto University, Japan
omura@rish.kyoto-u.ac.jp

1 Introduction

The basic techniques and important concepts of the one-dimensional electromagnetic particle code: KEMPO1 [*Omura and Matsumoto*, 1993] are reviewed briefly in this article. In the code, Maxwell's equations and equations of motions for a large number of superparticles are solved. Because of the limitation in the number of superparticles, electrostatic thermal fluctuations are enhanced in the particle code, which often interfere with physical processes to be reproduced in simulations. From a simplified analysis of the fluctuations, a criterion for the ratio of the grid spacing to the Debye length is given. A modification of the KEMPO1 for the solution of the relativistic equations of motion is also described. Since essential parts of the code are very simple and short, it is easy to modify the code regarding the initialization and the boundary conditions. To facilitate modification of the code and its verification by graphic outputs, we have rewritten the KEMPO1 code using the MATLAB programming software. MATLAB provides us with a convenient graphic user interface and flexible graphic diagnostics. Explanation of the input parameters for the relativistic KEMPO1/MATLAB code and several examples of applications are given for tutorial purposes.

2 Basic Equations and Methods of Computation

Electromagnetic processes in space plasmas are governed by Maxwell's equations:

$$\nabla \times \boldsymbol{B} = \mu_0 \boldsymbol{J} + \frac{1}{c^2} \frac{\partial \boldsymbol{E}}{\partial t} \tag{1}$$

$$\nabla \times \boldsymbol{E} = -\frac{\partial \boldsymbol{B}}{\partial t} \tag{2}$$

$$\nabla \cdot \boldsymbol{E} = \frac{\rho}{\varepsilon_o} \tag{3}$$

$$\nabla \cdot \boldsymbol{B} = 0 \tag{4}$$

where $\boldsymbol{J}$, ρ, c, ε_o, and μ_0 are the current density, charge density, light speed, electric permittivity, and magnetic permeability, respectively. In simulations the values of the

permittivity ε_0 and permeability μ_0 can be defined arbitrarily, as long as they satisfy the relation

$$\varepsilon_0\mu_0 = \frac{1}{c^2}. \tag{5}$$

In the KEMPO1, for simplicity, we adopt the following definition

$$\varepsilon_0 = 1, \qquad \mu_0 = \frac{1}{c^2}.$$

We solve Maxwell's equations for the electric field $\boldsymbol{E} \equiv (E_x, E_y, E_z)$ and magnetic field $\boldsymbol{B} \equiv (B_y, B_z)$ in a one-dimensional system. It is noted that B_x is a constant in the one-dimensional system because of (4). In a vacuum without any charged particles, we have $\boldsymbol{J} = 0$. The set of Maxwell's equations (1) and (2) are solved by the standard FDTD (Finite Difference Time Domain) method, which has been used widely in the various field of radio science.

We introduce two sets of spatial grid systems along the x-axis. One is a full-integer grid system defined at $i\,\Delta x$ ($i = 1, 2, 3, ..., Nx$) and the other is a half-integer grid system at $(i + 1/2)\Delta x$. We define E_y, B_y, J_y, and ρ on the full-integer grids, and E_x, E_z, B_z, J_x on the half-integer grids. We replace spatial and time derivatives in Maxwell's equations with the following centered differences by Δx and the time step Δt.

$$\frac{B_{y,i+1} - B_{y,i}}{\Delta x} = \mu_o J_{z,i+1/2} \tag{6}$$

$$\frac{B_{z,i+1/2} - B_{z,i-1/2}}{\Delta x} = -\mu_o J_{y,i} \tag{7}$$

$$E(X_i, t) = E_o \exp(kX_i - \omega t) \tag{8}$$

$$\begin{aligned}
\frac{\partial E(X_i, t)}{\partial x} &= \frac{E(X_i + \Delta x/2, t) - E(X_i - \Delta x/2, t)}{\Delta x} \\
&= \frac{1}{\Delta x}[\exp(k\Delta x/2) - \exp(-k\Delta x/2)]\,E(X_i, t) \\
&= i\frac{\sin(k\Delta x/2)}{\Delta x/2}E(X_i, t) = iKE(X_i, t)
\end{aligned} \tag{9}$$

where

$$K = \frac{\sin(k\Delta x/2)}{\Delta x/2} \tag{10}$$

Because of the centered difference scheme, the dispersion relation of electromagnetic waves in a vacuum $\omega^2 = c^2k^2$ is replaced by a modified dispersion relation

$$\Omega^2 = c^2K^2 \tag{11}$$

where Ω is given by

$$\Omega = \frac{\sin(\omega \Delta t/2)}{\Delta t/2}. \tag{12}$$

This gives the Courant condition for the time step and the grid spacing,

$$c\Delta t < \Delta x. \tag{13}$$

If the Courant condition is violated, the electromagnetic field grows exponentially because of the imaginary part of ω as a solution of (12).

In the presence of charged particles, we need to compute the charge density and the current density to incorporate their effects on the electromagnetic field. The charge density ρ_i on a grid point at $x = X_i$ is calculated by

$$\rho_i = \frac{1}{\Delta x} \sum_{j}^{N_p} q_j W(x_j - X_i) \tag{14}$$

where W_x is a particle shape function given by

$$
\begin{aligned}
W(x) &= 1 - \tfrac{|x|}{\Delta x}, \ |x| \le \Delta x \\
&= \quad 0, \quad |x| > \Delta x
\end{aligned}
\tag{15}
$$

The summation in (14) is taken for all N_p particles in the simulation system.

The initial electric field E_x is calculated from (3) in the difference form

$$\frac{E_{x,i+1/2} - E_{x,i-1/2}}{\Delta x} = \frac{\rho_i}{\varepsilon_0} \tag{16}$$

where ε_0 is the electric permittivity.

The current density J_x is calculated based on the charge conservation method [*Villasenor and Buneman*, 1992; *Umeda et al.*, 2003] satisfying the continuity equations of the charge,

$$J_{x,i+1/2}^{t+\Delta t/2} - J_{x,i-1/2}^{t+\Delta t/2} = -\frac{\Delta x}{\Delta t}(\rho_i^{t+\Delta t} - \rho_i^t). \tag{17}$$

The current densities J_y and J_z are calculated by

$$\boldsymbol{J}_{i+1/2}^{t+\Delta t/2} = \frac{1}{\Delta x} \sum_{j}^{N_p} q_j \boldsymbol{v} W(x_j - X_{i+1/2}). \tag{18}$$

The values of J_y calculated at the half-integer grids are relocated to the full-integer grids by the following procedure:

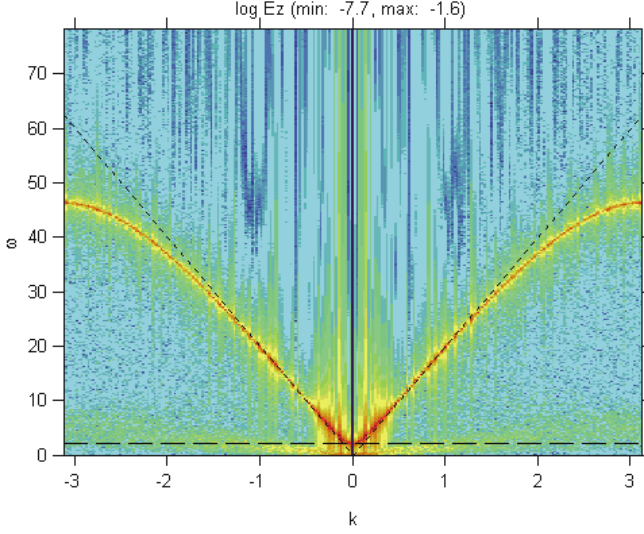$$J_{y,i} = \frac{J_{y,i-1/2} + J_{y,i+1/2}}{2}. \tag{19}$$

Fig. 1.   Dispersion relation of the thermal noise in an unmagnetized plasma.

With these components of the current density $\boldsymbol{J}$, we can trace time evolution of electromagnetic fields $\boldsymbol{E}$ and $\boldsymbol{B}$ by solving Maxwell's equations with the FDTD method.

In Fig. 1, we plotted frequency ω and wavenumber k spectra of an electromagnetic component E_z obtained by a run of the KEMPO1 code. The electromagnetic fluctuation is induced by the current densities due to the thermal motion of the plasma. Using the technique of the fast Fourier transform (FFT), we have applied the discrete Fourier transform to the electric field component E_z in space and time. The forward and backward traveling waves are separated by positive and negative wavenumbers, respectively. The separation technique is described in *Matsumoto and Omura* [1985]. As we find in the modified dispersion relation due to the centered difference scheme described above, the high frequency part of the dispersion relation of electromagnetic waves deviates from the oblique dashed lines representing the speed of light. The holizontal dashed line indicates the electron plasma frequency.

Since the current density J_x exactly satisfies the continuity equations of the charge density, E_x updated by the current density J_x automatically satisfy (16), if the difference equation is satisfied initially.

The equations of motion for a particle with a charge q and a mass m are the following:

$$\frac{\mathrm{d}\boldsymbol{v}}{\mathrm{d}t} = \frac{q}{m}(\boldsymbol{E} + \boldsymbol{v} \times \boldsymbol{B}), \qquad (20)$$

$$\frac{\mathrm{d}x}{\mathrm{d}t} = v_x \tag{21}$$

Equation (20) is solved by the Buneman-Boris method [*Hockney and Eastwood*, 1981; *Birdsall and Langdon*, 1985]. The advantage of the method is that it maintains strict conservation of the kinetic energy in the calculation of cyclotron motion. Even with a relatively large time step $\omega_c \Delta t$, the kinetic energy is strictly conserved. The angular cyclotron frequency Ω_c given by

$$\Omega_c = \frac{\tan^{-1} \omega_c \Delta t / 2}{\Delta t / 2} \tag{22}$$

is slightly decreased as the time step becomes large. In most of the applications the decrease can be neglected because $\Omega_c / \omega_c = 0.9967$ with $\omega_c \Delta t = 0.2$. In advancing the velocity $\boldsymbol{v}$ from $t - \Delta t / 2$ to $t + \Delta t / 2$, we need the electric field $\boldsymbol{E}$ and magnetic field $\boldsymbol{B}$ at time t at particle position $x(t)$. We interpolate the field linearly from the values at the adjacent grid points. It is interesting that the linear interpolation can be expressed by the following two equations with the same shape function $W(x)$ used for calculation of the charge and current densities. We use

$$F(x) = \sum_{i=1}^{N_x} F_i W(x - X_i) \tag{23}$$

for the fields defined $\{F_i\}$ at the full-integer grids, while we use

$$H(x) = \sum_{i=1}^{N_x} H_{i+1/2} W(x - X_{i+1/2}) \tag{24}$$

for the fields $\{H_{i+1/2}\}$ defined at the half-integer grids, where N_x is the total number of grid points in the system.

The electrostatic component E_x defined at the half-integer grids, however, has to be relocated to the full-integer grids before the interpolation by the following procedure:

$$E_{x,i} = \frac{E_{x,i-1/2} + E_{x,i+1/2}}{2} \tag{25}$$

This is done in order to cancel the electrostatic self-force [*Matsumoto and Omura*, 1985]. Since the source of the electrostatic field is the charge density ρ defined at the full-integer grids, the force interpolation must also be made from the full-integer grids by (23). A particle should not be influenced by the field due to its own charge. Similarly, the magnetic field B_y has to be relocated before the interpolation from the full-integer grids to the half-integer grids by

$$B_{y,i+1/2} = \frac{B_{y,i} + B_{y,i+1}}{2}. \tag{26}$$

This is for cancellation of the magnetostatic self-force due to the current density J_z, i.e., Ampere's law:

$$\frac{B_{y,i+1} - B_{y,i}}{\Delta x} = \mu_o J_{z,i+1/2} \tag{27}$$

It is noted that both J_y and J_z are calculated at the half-integer grids. In summary, E_x and E_y are interpolated from the full-integer grids, while E_z, B_y, and B_z are interpolated from the half-integer grids.

3   Relativistic KEMPO1

For high energy particles with velocity close to the speed of light, we solve the relativistic equation of motion,

$$\frac{d}{dt}(m\boldsymbol{v}) = q\,(\boldsymbol{E} + \boldsymbol{v} \times \boldsymbol{B}) \tag{28}$$

where $m = \gamma m_0$, m_0 is the mass at rest, and γ is the Lorentz factor given by

$$\gamma = \frac{1}{\sqrt{1 - \left(\frac{v}{c}\right)^2}}. \tag{29}$$

We define $\boldsymbol{u} = \gamma \boldsymbol{v}$, or

$$\boldsymbol{u} = \frac{c}{\sqrt{c^2 - |\boldsymbol{v}|^2}}\boldsymbol{v}. \tag{30}$$

Solving for $\boldsymbol{v}$, we have

$$\boldsymbol{v} = \frac{c}{\sqrt{c^2 + |\boldsymbol{u}|^2}}\boldsymbol{u}. \tag{31}$$

Equation (28) is rewritten as

$$\frac{d\boldsymbol{u}}{dt} = \frac{q}{m_0}\left(\boldsymbol{E} + \frac{c}{\sqrt{c^2 + |\boldsymbol{u}|^2}}\boldsymbol{u} \times \boldsymbol{B}\right). \tag{32}$$

Defining a modified magnetic field as

$$\boldsymbol{B}_u = \frac{c}{\sqrt{c^2 + |\boldsymbol{u}|^2}}\boldsymbol{B}, \tag{33}$$

we obtain the equation,

$$\frac{d\boldsymbol{u}}{dt} = \frac{q}{m_0}\,(\boldsymbol{E} + \boldsymbol{u} \times \boldsymbol{B_u}) \tag{34}$$

which is the same form as (20). The difference form of this equation is

$$\frac{\boldsymbol{u}^{t+\Delta t/2} - \boldsymbol{u}^{t-\Delta t/2}}{\Delta t} = \frac{q}{m_0}\left(\boldsymbol{E}^t + \frac{\boldsymbol{u}^{t+\Delta t/2} + \boldsymbol{u}^{t-\Delta t/2}}{2} \times \boldsymbol{B}_u^t\right) \tag{35}$$

We can apply the Buneman-Boris method specified as follows:

Step 1:

$$\boldsymbol{u}^{t-\Delta t/2} = \frac{c}{\sqrt{c^2 - \left|\boldsymbol{v}^{t-\Delta t/2}\right|^2}} \boldsymbol{v}^{t-\Delta t/2} \tag{36}$$

Step 2:

$$\boldsymbol{u}_1^t = \boldsymbol{u}^{t-\Delta t/2} + \frac{q}{m_0} \frac{\Delta t}{2} \boldsymbol{E}^t \tag{37}$$

Step 3:

$$\boldsymbol{B}_u^t = \frac{c}{\sqrt{c^2 + \left|\boldsymbol{u}_1^t\right|^2}} \boldsymbol{B}^t \tag{38}$$

Step 4:

$$\boldsymbol{u}^{t'} = \boldsymbol{u}_1^t + \frac{q}{m_0} \frac{\Delta t}{2} \boldsymbol{u}_1^t \times \boldsymbol{B}_u^t \tag{39}$$

Step 5:

$$\boldsymbol{u}_2^t = \boldsymbol{u}_1^t + \frac{2}{1 + \left(\boldsymbol{B}_u^t \frac{q}{m_0} \frac{\Delta t}{2}\right)^2} \boldsymbol{u}^{t'} \times \boldsymbol{B}_u^t \frac{q}{m_0} \frac{\Delta t}{2} \tag{40}$$

Step 6:

$$\boldsymbol{u}^{t+\Delta t/2} = \boldsymbol{u}_2^t + \frac{q}{m_0} \frac{\Delta t}{2} \boldsymbol{E}^t \tag{41}$$

Step 7:

$$\boldsymbol{v}^{t+\Delta t/2} = \frac{c}{\sqrt{c^2 + \left|\boldsymbol{u}^{t+\Delta t/2}\right|^2}} \boldsymbol{u}^{t+\Delta t/2} \tag{42}$$

In (38), $\boldsymbol{B}_u^t$ is computed from $\boldsymbol{u}_1^t$ and $\boldsymbol{B}^t$, because

$$\left|\boldsymbol{u}^{t+\Delta t/2} + \boldsymbol{u}^{t-\frac{\Delta t}{2}}\right| = \left|\frac{\boldsymbol{u}_1^t + \boldsymbol{u}_2^t}{2}\right| \tag{43}$$

and $|\boldsymbol{u}_1^t| = |\boldsymbol{u}_2^t|$.

In the relativistic code, we initialize particle velocities so that the following distribution function is realized in the momentum space (u_x, u_y, u_z)

$$f(u_\parallel, u_\perp) \propto \exp\left(-\frac{(u_\parallel - V_{d\parallel})^2}{2V_{t\parallel}^2} - \frac{(u_\perp - V_{d\perp})^2}{2V_{t\perp}^2}\right) \tag{44}$$

With $V_{d\perp} = 0$, the distribution function is reduced to the shifted bi-Maxwellian distribution, while a finite $V_{d\perp}$ ($>> V_{t\perp}$) realizes a ring distribution. Using a random number generator for the standard normal distribution, we assign each particle a momentum $\boldsymbol{u} = (u_x, u_y, u_z)$, which is converted to a velocity $\boldsymbol{v} = (v_x, v_y, v_z)$ by (31), namely,

$$\boldsymbol{v} = \boldsymbol{u}/\gamma = \frac{c}{\sqrt{c^2 + u_x^2 + u_y^2 + u_z^2}} \boldsymbol{u} \tag{45}$$

As one of the diagnostics, the kinetic energy of each particle is calculated by

$$T_E = mc^2 - m_0c^2$$
$$= (\gamma - 1)m_0c^2. \tag{46}$$

The sum of the kinetic energy is taken for all particles in the simulation system. We divide the sum by the length of the system to obtain the average kinetic energy density. The sums of the electric and magnetic field energies are taken for all grid points forming the simulation system. Dividing them by the number of grid points, we obtain the average electric and magnetic field energy densities in the system.

4 Thermal Fluctuation

Each superparticle in the particle code has a much larger kinetic energy than a real charged particle in a real space plasma. The number of particles in the Debye length is much smaller than that in a real space plasma. This results in enhanced thermal fluctuations of the electrostatic field. The electrostatic field energy density of the thermal fluctuation F_E is given by

$$F_E = \frac{T}{2} \int_{-\infty}^{\infty} \frac{1}{1 + k^2\lambda_D^2} \frac{dk}{2\pi}$$
$$= \frac{T}{4\lambda_D} \tag{47}$$

where $T \, (\equiv mV_t^2)$ is the temperature in the dimensions of energy. The thermal energy density, on the other hand, is given by,

$$T_E = \frac{1}{2}nT. \tag{48}$$

We obtain the ratio of the electrostatic field energy density F_E to the thermal energy density T_E as expressed in terms of the number of particles per cell and the ratio of the Debye length to the grid spacing, thus:

$$\frac{F_E}{T_E} = \frac{1}{2}\frac{1}{n\lambda_D}$$
$$= \frac{1}{2}\frac{N_x}{N_p}\frac{\Delta x}{\lambda_D} \tag{49}$$

In the presence of a fluctuation $\delta\phi$ of the electrostatic potential, we have the density fluctuation approximated by

$$n \sim n_0 \exp(-\frac{q\delta\phi}{T}). \tag{50}$$

If we insert relation (50) into Poisson's equation, we have

$$\frac{\partial^2 \delta\phi}{\partial x^2} \sim \frac{q^2 n}{\varepsilon_o T}\delta\phi = \frac{\omega_p^2}{V_t^2}\delta\phi = \frac{1}{\lambda_D^2}\delta\phi. \tag{51}$$

Applying Fourier transformation, we obtain

$$(k^2 - \frac{1}{\lambda_D^2})\delta\phi_k \sim 0 \tag{52}$$

In order to have a finite $\delta\phi_k$, we must set,

$$|k| \sim \frac{1}{\lambda_D}. \tag{53}$$

Because we choose the difference scheme in calculating the spatial derivatives, the wavenumber k is replaced by K given by (10). Multiplying $\Delta x/2$, we obtain

$$|\sin(k\Delta x/2))| \sim \frac{\Delta x}{2\lambda_D}. \tag{54}$$

In order to satisfy the above relation, the following condition must be satisfied:

$$\Delta x < 2\lambda_D \tag{55}$$

A detailed study of thermal fluctuations has been conducted with the KEMPO1 code [*Ueda et al.*, 1994]. If the condition is violated, there arises a nonphysical numerical heating with a large growth rate. The heating continues, and the effective Debye length increases until the condition (55) is satisfied.

5   Input Parameters

The following is the list of parameters used in the KEMPO1/MATLAB code. These parameters are specified through a graphic user interface as shown in Fig. 2. A set of default parameters is automatically loaded from a file named "default.dat," which has been installed in the KEMPO1 work directory. Different sets of parameters can be loaded from other parameter files in the directory by the "LOAD" button at the bottom. The current parameters can be saved to a specified file by the "SAVE" button.

- DX: Grid spacing.

- DT: Time step.

- CV: Speed of light

- WC: Cyclotron frequency of species 1, ω_{c1}. From this cyclotron frequency, we compute the magnitude of the static magnetic field B_o from the relation of $B_o = \omega_{c1}/(q/m)_1$.
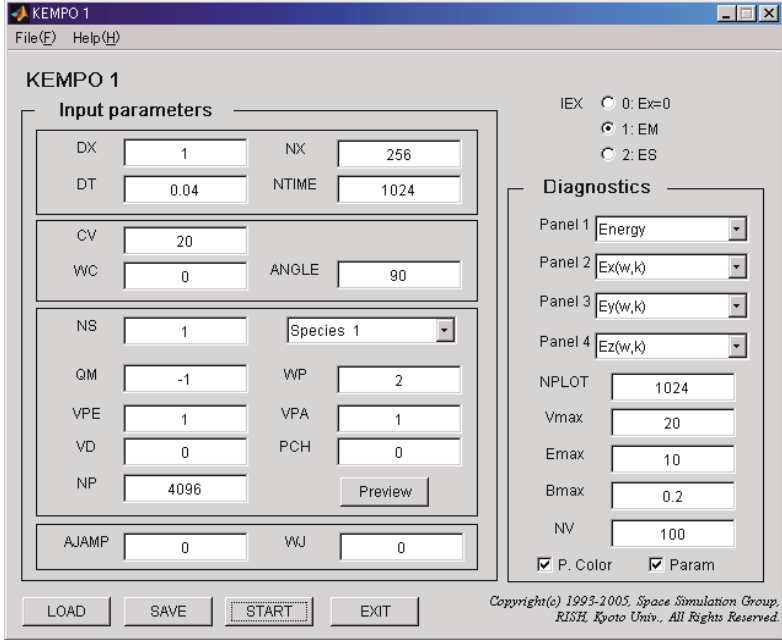
Fig. 2.   Graphical User Interface for specifying a set of parameters of KEMPO1. The four buttons at
the bottom are for loading a set of parameters from a file, saving the current parameters, starting the
simulation, and terminating the program.

- *ANGLE*: Angle between the static magnetic field $\boldsymbol{B}_o$ and the wave Vector $\boldsymbol{k}$.
  The static magnetic field $\boldsymbol{B}_o$ is taken in the x-y plane.

- *NX*: Number of grid points N_x.

- *NTIME*: Number of time steps in a simulation run.

- *NS*: Number of particle species.

- *QM(i)*: Charge-to-mass ratio q_i/m_i of species i

- *WP(i)*: Plasma frequency of species i defined by

$$\omega_{pi} = \sqrt{\frac{n_i q_i^2}{m_i}} \tag{56}$$

where n_i, q_i, and m_i are number density, charge and mass of species i, respectively. We calculate the average number density by

$$n_i = \frac{N_p}{N_x \Delta_x} \tag{57}$$

and determine the charge of a superparticle by

$$q_i = \frac{\rho_i}{n_i} = \frac{\omega_{pi}^2}{(q_i/m_i)n_i}. \tag{58}$$

In a system with ions as mobile particles, the following charge neutrality condition must be satisfied:

$$\sum_i \rho_i = \sum_i q_i n_i = \sum_i \frac{\omega_{pi}^2}{q_i/m_i} = 0 \tag{59}$$

In a system with mobile electrons only, the charge density of the background immobile ions is automatically computed to establish charge neutrality.

- $VPE(i)$; Perpendicular thermal velocity of species i.

- $VPA(i)$; Parallel thermal velocity of species i.

- $VD(i)$: Drift velocity of species i. In combination with the pitch angle $\phi = PCH(i)$, the drift velocities of parallel and perpendicular components are determined.

$$V_{d\perp} = V_d \sin \phi \tag{60}$$

$$V_{d\parallel} = V_d \cos \phi \tag{61}$$

- $PCH(i)$: Pitch angle ϕ (degrees) of species i defining parallel and perpendicular drift velocities $V_{d\parallel}$ and $V_{d\perp}$.

- $NP(i)$: Number of superparticles for species i in the simulation system.

- $AJAMP$: The amplitude of an external current $J_{z,\text{ext}}$ placed at the center of the simulation system.

- WJ : The frequency of the external current $J_{z,\text{ext}}$.

- IEX: Control parameter for electrostatic option. If $IEX = 0$, the electrostatic component E_x is not solved. If $IEX = 1$, both electromagnetic and electrostatic components are solved. If $IEX = 2$, the electromagnetic components are not solved. Instead of Maxwell's equations, Poisson's equation is solved along with calculation of the charge density.

- $NPLOT$: Number of diagnostics to be made throughout the simulation run. In the KEMPO1/MATLAB interface windows, we can specify four different diagnostics to be made at a time interval of $\Delta t \times NTIME/NPLOT$. The following diagnostics are available.

  - 2D phase space plot of particles in (V_x, x), (V_y, x), or (V_z, x)
  - 3D velocity space plot of particles in (V_x, V_y, V_z)

- Plot of $E_x(x)$, $E_y(x)$, $E_z(x)$, $B_y(x)$, or $B_z(x)$
- 3D plots of transverse fields (E_y, E_z), (B_y, B_z), and perpendicular parti-
  cle velocities (V_y, V_z) along the x-axis. The transverse scales for veloc-
  ities, electric fields, and magnetic fields, are normalized by V_{max}, E_{max},
  and B_{max}, respectively.
- Wavenumber spectrum of $E_x(k)$, $E_y(k)$, $E_z(k)$, $B_y(k)$, or $B_z(k)$
- ω-k diagram of E_x, E_y, E_z, B_y, and B_z.
- Contour plot of E_x, E_y, E_z, B_y, and B_z.
- Energy history plot of kinetic, electric, and magnetic energy densities
- Distribution function of $f(V_x)$, $f(V_y)$, or $f(V_z)$ for electrons and ions.

In the panel of the diagnostics parameters, options of "P.Color" and "Param" can be
specified. "P.Color" makes particles plotted in color, and "Param" makes the param-
eters such as the speed of light, the initial drift velocity, the cyclotron frequency, the
plasma frequencies, and the initial velocity distributions plotted in the diagnostics.

It is noted that all physical parameters are determined with reference to the speed
of light c and a characteristic frequency ω of the simulation system such as the elec-
tron plasma frequency ω_{pe} or the electron cyclotron frequency ω_{ce}. Once the values
of these quantities are given, we can choose the time step Δt so that it satisfies

$$\omega \Delta t << 2\pi. \tag{62}$$

We normally set $\max(\omega_{pe}, \omega_{ce}) \sim 0.1$ for accurate reproduction of the oscillation
with a reasonably short computation time.. In combination with Δt, the grid spacing
Δx should be determined so that the set of Maxwell's equations can be integrated
stably in time.

6   Exercises

We study several examples of particle simulations using the KEMPO1/MATLAB
code. Thanks to the advanced capability of personal computers and efficiency of the
MATLAB software, we can perform various test runs that facilitate our understanding
of the basic processes in space plasmas such as wave instabilities [e.g., *Gary*, 1993]
and their nonlinear evolutions. In the following, we will go through basic tests of the
simulation code with emphasis on its numerical property.

6.1   Electrostatic thermal fluctuations

As we have seen in Eq. (47), thermal motion of electrons gives a fluctuation of
electrostatic field. We check the condition on the Debye length and the grid spacing
by varying the ratio $\lambda_D/\Delta x = VPA/(WPDX)$. We can find a distinct difference
between 0.5 and 0.2 after running the code with $WP = 1$, $DT = 0.1$, $DX = 1$,
$NX = 128$, $NP = 128$, and $NTIME = 4096$. In both cases, the thermal energy
increases due to the electrostatic fluctuations. The rates of the energy increase are,
however, clearly different. The energy increase indicates that the fluctuation with the
smaller value of $\lambda_D/\Delta x$ is nonphysical, resulting in stochastic heating of particles.

Although the code can be run with the electrostatic option $IEX = 2$, it may also be run as the full electromagnetic option $IEX = 1$. The Courant condition (13) must strictly be satisfied, i.e., $CV < DX/DT = 10$. As a test, one may try violation of this condition. It is also useful to confirm that the ratio of the electrostatic energy to the thermal energy is inversely proportional to NP/NX. To study coherent wave phenomena in space plasmas by the particle code, we generally need a large number of superparticles.

6.2 ω-k dispersion relations of plasma waves

We have prepared a spectrum analysis program that generates ω-k diagrams by applying discrete Fourier transformations in space and time. The forward and backward traveling waves are separated by positive and negative wavenumbers, respectively. The technique is described in *Matsumoto and Omura* [1985]. We can reproduce the dispersion relations of various plasma waves by giving enough resolutions in space and time. We need to give a sufficient number of superparticles to form the Maxwellian velocity distribution functions within one wavelength of the wave of interest. It is suggested to try the following parameters with the options for diagnostics "Ex(w,k)","Ey(w,k)", "By(w,k)", and "Energy" for panels 1, 2, 3, and 4, respectively. The code must be executed as the full electromagnetic code with the option $IEX = 1$. A set of interesting $\omega - k$ diagrams can be obtained with $DX = 1$ $NX = 256, DT = 0.1, NTIME = 1024, CV = 8, WC = -1, NS = 1, WP = 2$, $NP = 1024$ and $NPLOT = 1024$. We can reproduce a variety of plasma dispersion relations by varying the propagation angle $ANGLE$ from 0 to 90 degrees. In Fig. 3, we have plotted the results of a run for waves propagating parallel to the static magnetic field. The upper right panel shows the ω-k diagram of the electrostatic component E_x. The mode at the plasma frequency $WP = 2$ corresponds to Langmuir waves. The lower panels show the transverse electric field E_y and magnetic field B_y. We can find R-mode and L-mode waves whose phase velocities approach the speed of light, and a whistler mode wave below the electron cyclotron frequency $|WC| = 1$. When we change the angle of the static magnetic field to 90 degrees as shown in Fig. 4, the electrostatic mode E_x shows the dispersion relations of electrostatic cyclotron waves called Bernstein modes. These include the upper hybrid waves that approach the upper hybrid resonance frequency $\sqrt{WP^2 + WC^2}$. The lower left panel show the electric field E_y in the direction of the magnetic field, which are called ordinary modes. The strong mode is an O-mode wave with its phase velocity approaching the speed of light, while the weak emissions with much smaller group velocities $\partial\omega/\partial k$ are O-mode cyclotron waves. The lower right panel shows extraordinary modes corresponding to those in the upper right panel. Execution of the code with these parameters takes substantial CPU time with Pentium or Athlon processors. We can monitor the execution by the energy history plot in the upper right panels of Figs. 3 and 4, but the ω-k diagrams appear only after completion of the run. It is also noted that dispersion relations of the light modes whose phase velocity approaches the speed of light are distorted at the high wavenumber range close to the wavenumber $k_{\max} = \pi/\Delta X$. This is due to the difference scheme as expressed by (11).
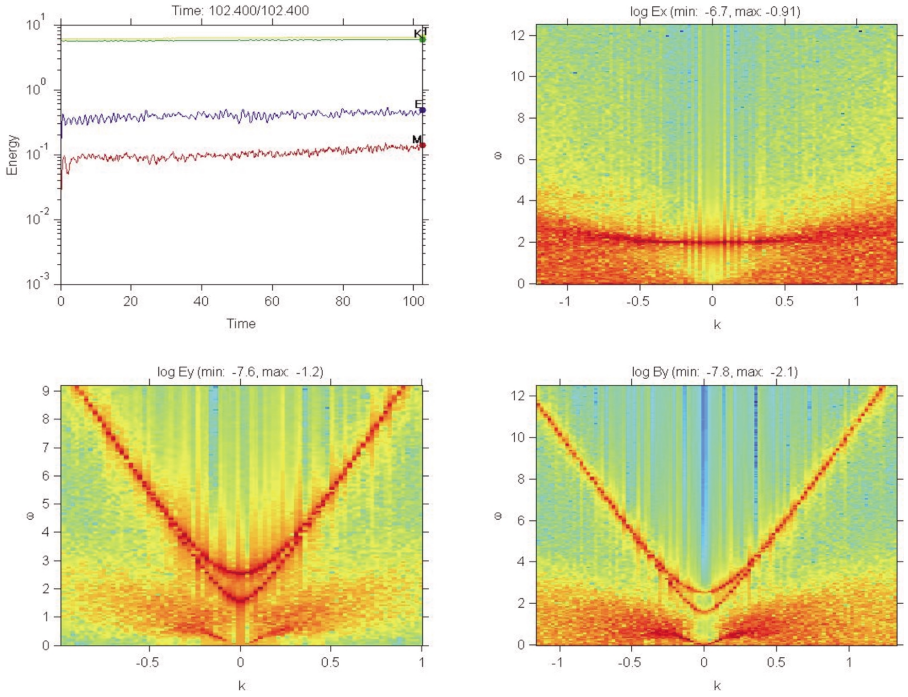
Fig. 3. ω-k dispersion relations of plasma waves propagating parallel to the static magnetic field (Exercise 5.2 for $ANGLE = 0$).

6.3   Propagation of electromagnetic waves

We can radiate electromagnetic waves from an antenna in plasmas. We have prepared an external current source at the center of the simulation system. The current source is directed in the z-axis direction. A finite amplitude should be applied to $AJAMP$ to turn on the current source. The current source is mathematically expressed by the Dirac delta-function δ as

$$J_{z,\text{ext}} = J_0 \Delta x \, \delta(x - X_{Nx/2}) \sin(\omega_J t). \tag{63}$$

where J_0 and ω_J are specified by $AJAMP$ and WJ, respectively. The solution of Maxwell's equations with the current (63) in vacua can be obtained analytically, and we can estimate the amplitude by

$$|E_{z,\text{max}}| = \frac{J_0 \Delta x}{2c}. \tag{64}$$

In a plasma, however, the electrons and ions respond to the field excited by the external current, and various normal modes we have seen in the ω-k diagrams can be excited depending on the frequency ω_J. In order to suppress the effect of the enhanced electrostatic fluctuation, we set $E_x = 0$ throughout the runs by specifying

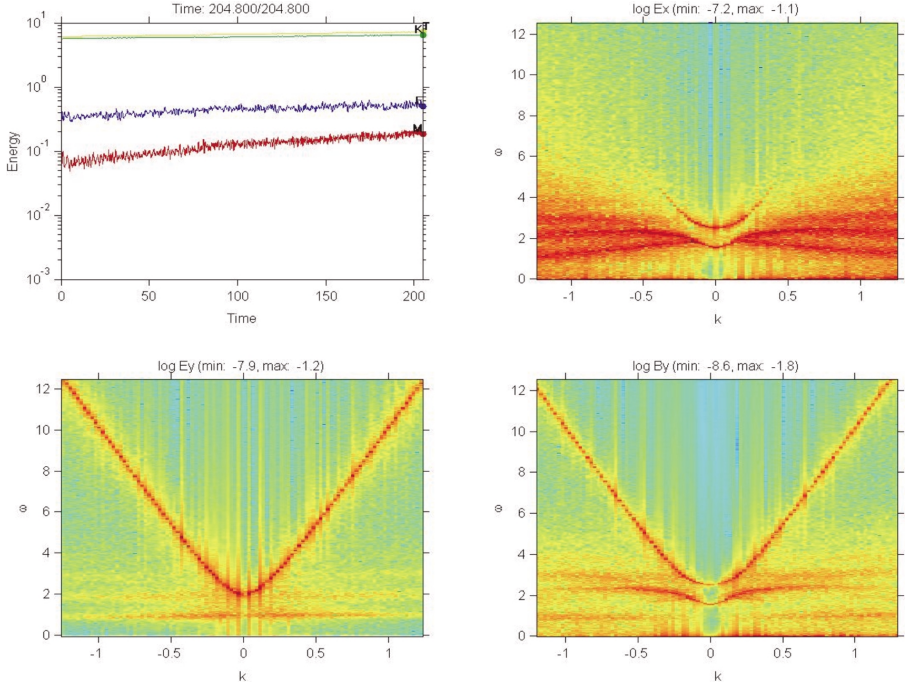Fig. 4. ω-k dispersion relations of plasma waves propagating perpendicular to the static magnetic field (Exercise 5.2 for $ANGLE = 90$).

$IEX = 0$. We use the following parameters: $DX = 1$, $NX = 1024$, $DT = 0.04$, $CV = 20$, $WP = 2$, $VPE = 0.01$, $VPA = 0.01$, $EMAX = 1$, $BMAX = 0.05$, $VMAX = 1$, and $NTIME = 1024$. By comparing the response of an unmagnetized plasma ($WC = 0$) and that of a magnetized plasma ($WC = -1.0$ and $ANGLE = 0$), we can find different polarizations of the electromagnetic waves. In the magnetized plasma, a whistler mode wave can be excited with $WJ = 0.5$. In the three-dimensional plot of the transverse components of the waves and particles as functions of x, a diagnostics specified by "VyzEByz-X" shown in Fig. 5, we can find a spiral structure of the whistler mode wave. In these runs with particles of a very low temperature, the particles work as a fluid without any kinetic effects.

6.4   Two-stream instability and electron holes

We now introduce two different groups of electrons, while the ions are assumed to be a neutralizing background as in the preceding test runs. The two groups of electrons have different drift velocities in the direction parallel to the static magnetic field. If the thermal velocities of the electrons are much smaller than the relative drift velocity between the two groups of electrons, there arises a strong electrostatic instability. Since the instability is purely electrostatic, the code can be run with the
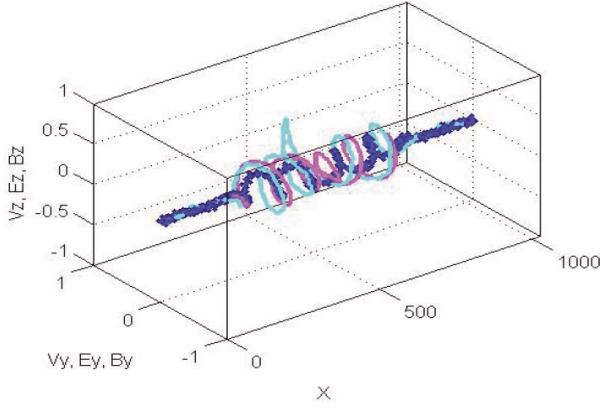
Fig. 5. Propagation of whistler mode wave from a thin current sheet embedded in a magnetized plasma.
Endpoints of vectors of the transverse magnetic fields (magenta) and electric fields (cyan) and perpen-
dicular velocities of particles (blue) are plotted from their origins on the x-axis.

electrostatic option $IEX = 2$ as well as the electromagnetic option $IEX = 1$. The
growth rate of the instability is large enough so that it can be demonstrated in spite
of large thermal fluctuations. The following parameters should be tried: $DX = 1$,
$NX = 64$, $DT = 0.04$, $CV = 20$, $NS = 2$, $WP = 2$, $PCH = 0$, $VPE =$
$VPA = 1$, $VD1 = 0$, $VD2 = 10$, $VMAX = 20$, and $EMAX = 10$. First we study
growth and saturation of the two-stream instability with $NP1 = NP2 = 256$ and
$NTIME = 256$. We find that a coherent electrostatic potential grows to trap most of
the electrons. The electrons undergo nonlinear oscillation in the potentials forming
vortices. The instability is saturated because of the mixing of the two streams of
electrons. Second, we try a long run with $NTIME = 2048$, keeping the same
number of particles $NP1 = NP2 = 256$. We find that the phase mixing continues
through the dissipation of the trapping potentials. Third, we increase the number
of particles in order to lower the thermal noise level by setting $NP1 = NP2 =$
4096, and run the code with $NTIME = 2048$. We find formation of very stable
potential structures through coalescence of smaller potentials as shown in Fig. 6.
These potential structures are called electron holes as found in the velocity phase
space plot of the upper left panel, or electrostatic solitary waves (ESW) as observed
in the lower left panel. There have been many observations, simulations, and theories
on ESW [*Matsumoto et al*., 1994; *Omura et al*., 1994, 1996; *Krasovsky et al*., 2003].
6.5   Whistler mode instability driven by temperature anisotropy

In the presence of highly anisotropic electrons as in the Earth's radiation belt,
whistler mode waves become unstable in the direction parallel to the static magnetic
field, diffusing the pitch angles of the energetic electrons through the cyclotron reso-
nance,
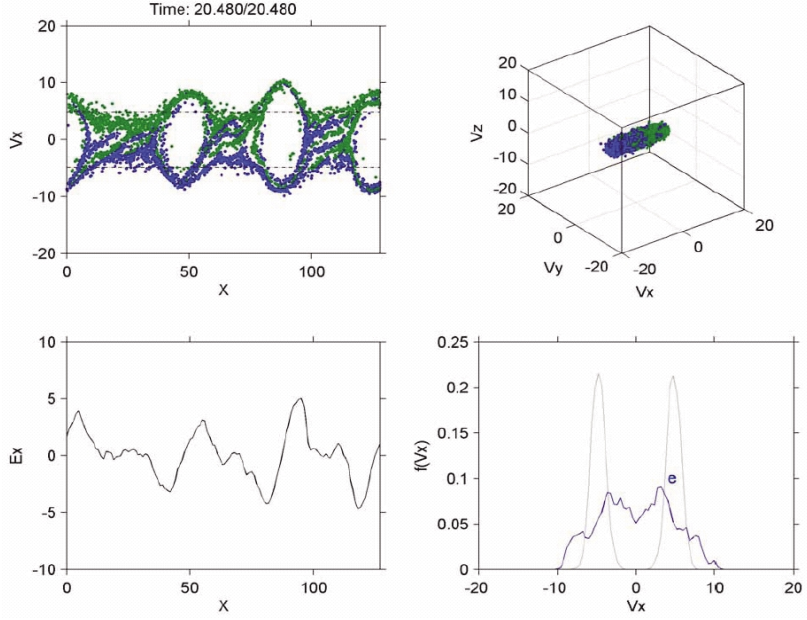
$$\omega - kv_\parallel = \omega_{ce}/\gamma \tag{65}$$

Fig. 6. Two-stream instability.

where ω_{ce} is the electron cyclotron frequency [*Kennel and Petschek*, 1966; *Omura and Summers*, 2004]. If the parallel velocity $v_\parallel$ of a high energy electron satisfies (65), the electron sees the stationary transverse electric field, exchanging energy with the transverse field. The parallel velocity $v_\parallel$, however, is affected by the enhanced thermal fluctuations of the parallel electrostatic fields that disturb an effective wave-particle interaction through the cyclotron resonance. Instead of suppressing the thermal fluctuation by assigning a large number of superparticles per grid, we can enforce $E_x = 0$ by setting the option $IEX = 0$. Let us compare two runs with $IEX = 0$ and $IEX = 1$. We assume two different species of electrons. One species is cold dense electrons, and the other is hot tenuous electrons. The following parameters are suggested: $DX = 1, NX = 256, DT = 0.04, NTIME = 4096, CV = 20, WC = -1, ANGLE = 0, NS = 2, QM = -1, WP1 = 2, WP2 = 0.5, VPE1 = VPA1 = 1, VPE2 = 20, VPA2 = 5, NP1 = NP2 = 4096$. We can find growth of whistler mode waves propagating both forward and backward along the magnetic field, i.e., the x axis, which we can confirm from the ω-k diagram of the transverse components B_y and B_z. Comparison with the linear growth rate of the whistler mode instability is found in *Omura and Summers* [2004].

6.6   Competing process of electrostatic instability and whistler mode instability

When an electron beam with a ring distribution in the perpendicular velocity is drifting along the static magnetic field, both a longitudinal electrostatic field and
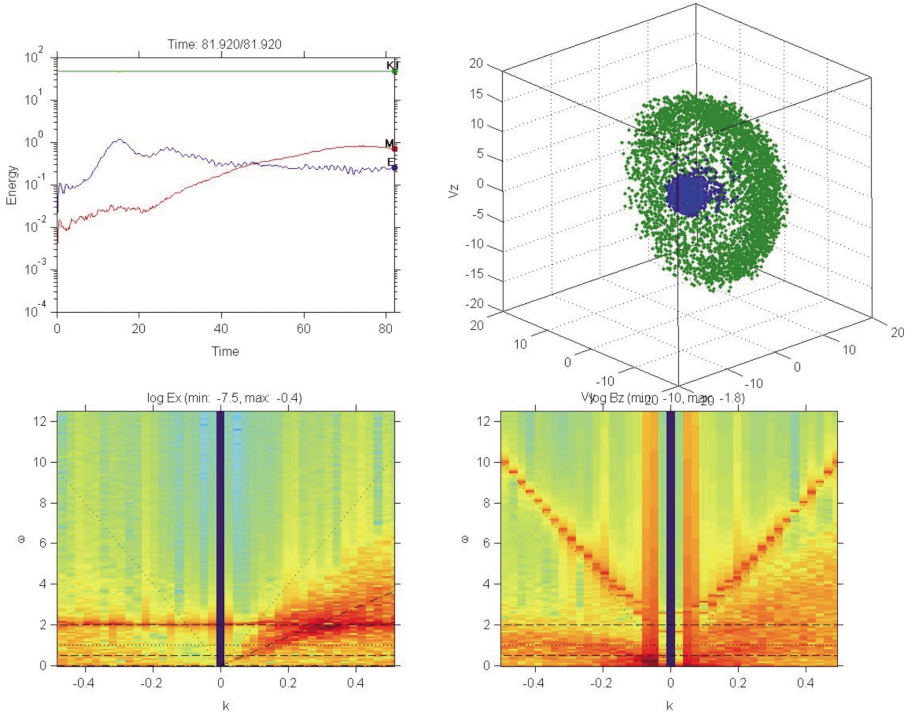
Fig. 7. Competing process of electrostatic instability and whistler mode instability.

transverse electromagnetic field are excited owing to an electrostatic beam instability and a whistler mode beam instability, respectively. The upper left panel of Fig. 7 shows time histories of the electric field energy, mostly consisting of that of the electrostatic E_x field, and the magnetic field energy of whistler mode wave. By plotting the ω-k diagram for E_x and B_z as in the lower panels of Fig. 7, we find that the directions of propagation are different for the electrostatic wave and the whistler mode wave. The following parameters are suggested: $DX = 1$, $NX = 256$, $DT = 0.04$, $NTIME = 2048$, $CV = 20$, $WC = -1$, $ANGLE = 0$, $NS = 2$, $QM = -1$, $WP1 = 2$, $WP2 = 0.5$, $VPE1 = VPA1 = VPE2 = VPA2 = 1$, $VD1 = 0$, $VD = 20$, $PCH2 = 60$. $NP1 = NP2 = 4096$. The diffusion process of the electron beam in the (V_x, V_y, V_z) phase space as shown in the upper right panel of Fig. 7 should be carefully examined.

It is also interesting to check the structure of the wave magnetic field, by specifying the three-dimensional plot of $v_{y,z}$, $B_{y,z}$, and $E_{y,z}$ along the x axis.

6.7 Buneman instability

When there arises a large-scale parallel electric field with a very low frequency, electrons are accelerated along the magnetic field forming a field-aligned current.
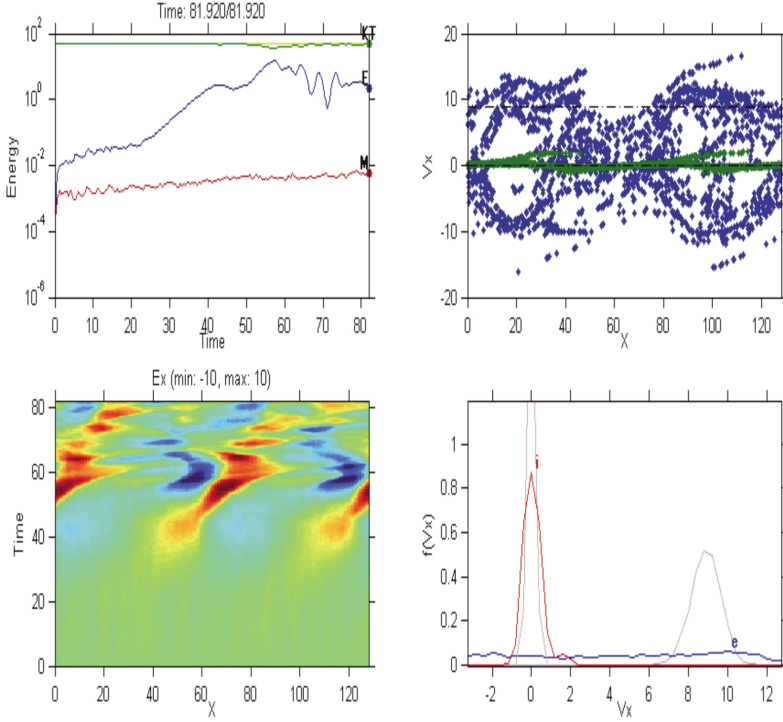
Fig. 8. Buneman instability.

In the presence of a large relative drift velocity $V_{t\parallel}$ between the thermal electrons and the thermal ions, a strong electrostatic instability called "Buneman instability" arises. The following parameters are suggested: $DX = 1$, $NX = 128$, $DT = 0.04$, $NTIME = 4096$, $CV = 20$, $WC = 0$, $ANGLE = 0$, $NS = 2$, $QM1 = -1$ $QM2 = 0.01$, $WP1 = 1$, $WP2 = 0.1$, $VPE1 = VPA1 = 1$, $VPE2 = VPA2 = 0.1$, $NP1 = NP2 = 2048$. As we find in the two-stream instability, the electrons are trapped by the growing electrostatic potential forming large electron holes or ESW, which subsequently decay into ion acoustic waves. The upper panels of Fig. 8 show the time history of the electrostatic field energy and electromagnetic field energy, and a snapshot of the phase diagram in $(v_\parallel, x)$ space showing both electrons and ions. The interaction is purely electrostatic, and we only have the E_x field component, which is plotted in the lower left panel of Fig. 8 as a function of space x and time t. The velocity distribution functions of electrons and ions are plotted as a snapshot at a specific time.

6.8   Electromagnetic ion cyclotron instability driven by an ion beam

The low frequency part of the whistler mode wave at a long wavelength is called an R-mode electromagnetic ion cyclotron wave (EMIC), which can be excited by an

ion beam with a drift velocity satisfying the anomalous cyclotron resonance condition

$$\omega - kv_{\parallel} = -\Omega_i \tag{66}$$

where Ω_i is the cyclotron frequency of ions [e.g., *Thorne and Tsurutani*, 1987; *Kojima et al.*, 1989]. The wave fields rotate around the static magnetic field in the same direction as electrons, but with a positive parallel velocity a few times greater than the Alfven velocity. The Doppler effect makes the beam ions see the wave fields rotate in the same direction as their cyclotron motion. In accordance with the anomalous cyclotron resonance condition, the ion beam can interact with the R-mode wave, giving its drift energy to the electromagnetic wave. The following parameters should be tried: $DX = 1$, $NX = 1024$, $DT = 0.45$, $NTIME = 4096$, $CV = 20$, $WC = -2.5$, $ANGLE = 0$, $NS = 3$, $QM1 = -1$, $QM2 = 0.04$, $QM3 = 0.04$, $WP1 = 10$, $WP2 = 1.789$, $WP3 = 0.8944$, $VPE1 = VPA1 = 2$, $VPE2 = VPA2 = VPE3 = VPA3 = 0.4$, $VD1 = VD2 = 0$, $VD3 = 15$, $NP1 = NP2 = NP3 = 524288$, and $IEX = 1$. In the very initial stage, the electrostatic Langmuir wave is excited by the ion beam, thermalizing the electrons in the parallel direction. The electromagnetic instability slowly proceed, scattering the beam ions in their pitch angles.

6.9   Electromagnetic ion cyclotron instability driven by temperature anisotropy of ions

L-mode ion cyclotron waves are excited through the cyclotron instability driven by energetic ions with temperature anisotropy ($T_{\perp}/T_{\parallel} > 1$) [*Gendrin et al.*, 1984], just as R-mode whistler mode waves are excited by anisotropic energetic electrons. It is noted that the instability excites both forward and backward traveling waves, which result in a standing wave with an amplitude modulated in space. The modulation results in a nonlinear Lorentz force in the direction of the static magnetic field [*Omura et al.*, 1988]. The L-mode dispersion relation will be split into two branches if there exists another species of heavy ions because of the cyclotron resonance with the heavy ions. The following parameters are suggested: $DX = 1$, $NX = 1024$, $DT = 0.45$, $NTIME = 4096$, $CV = 20$, $WC = 20$, $ANGLE = 0$, $NS = 3$, $QM1 = -1$, $QM2 = 0.04$, $QM3 = 0.04$, $WP1 = 10$, $WP2 = 1.732$, $WP3 = 1.0$, $VPE1 = VPA1 = 2$, $VPE2 = VPA2 = 0.4$, $VPE3 = 4$, , $VPA3 = 0.4$, $VD1 = VD2 = 0$, $VD3 = 15$, $NP1 = NP2 = NP3 = 524288$, and $IEX = 1$.

7   Concluding Remarks

There are many other interesting physical problems that can be studied by the KEMPO1/MATLAB code. I hope the code will be utilized for better understanding of basic microphysics and nonlinear processes in space plasmas.

References

Birdsall, C. K. and B. K. Langdon, *Plasma Physics via Computer Simulation*, McGraw-Hill, New York, 1985.

Gary, S. P., *Theory of Space Plasma Microinstabilities*, Cambridge University Press, 1993.

Gendrin, R., M. Ashour-Abdalla, Y. Omura, and K. Quest, Linear Analysis of Ion Cyclotron Interaction in a Multicomponent Plasma, *J. Geophys. Res.*, **89**, 9,119–9,124, 1984.

Hockney, R. W. and J. W. Eastwood, *Computer Simulation Using Particle*, McGraw-Hill, New York, 1981.

Kennel, C. F. and H. E. Petschek, Limit on stably trapped particle fluxes, *J. Geophys. Res.*, **71**, 1–28, 1966.

Kojima, H., H. Matsumoto, Y. Omura, and B. T. Tsurutani, Nonlinear Evolution of High-Frequency R-Mode Waves Excited by Water Group Ions Near Comets: Computer Experiments, *Geophys. Res. Lett.*, **16**, 9–12, 1989.

Krasovsky, V. L., H. Matsumoto, and Y. Omura, Electrostatic solitary waves as collective charges in a magnetospheric plasma: Physical structure and properties of Vernstein-Greene-Kruskal (BGK) solitons, *J. Geophys. Res.*, **108**(1117), doi:10.1029/2001JA000277, 2003.

Matsumoto, H. and Y. Omura, Particle simulations of electromagnetic waves and their applications to space plasmas, *Computer Simulations of Space Plasmas*, Edited by: H. Matsumoto and T. Sato, Terra Pub. and Reidel Co., 1985.

Matsumoto, H., H. Kojima, S. Miyatake, Y. Omura, Mokada, I. Nagano, and M. Tsutsui, Electrostatic Solitary Waves (ESW) in the Magnetotail: BEN Wave Forms Observed by GEOTAIL, *Geophys. Res. Lett.*, **21**, 2,915–2,918, 1994.

Omura, Y. and H. Matsumoto, KEMPO1: Technical guide to one-dimensional electromagnetic particle code, in *Computer Space Plasma Physic: Simulation Techniques and Softwares*, Edited by: H. Matsumoto and Y. Omura, Terra Scientific Pub., Tokyo, 1993.

Omura, Y. and D. Summers, Computer simulations of relativistic whistler-mode wave-particle interactions, *Physics of Plasmas*, **11**, 3530–3534, 2004.

Omura, Y., H. Usui, and H. Matsumoto, Parallel heating associated with interaction of forward and backward electromagnetic cyclotron waves, *J. Geomag. Geoelectr.*, **40**, 949–961, 1988.

Omura, Y., H. Kojima, and H. Matsumoto, Computer simulation of electrostatic solitary waves: A nonlinear model of broadband electrostatic noise, *Geophys. Res. Lett.*, **21**, 2,923–2,926, 1994.

Omura, Y., H. Matsumoto, T. Miyake, and H. Kojima, Electron Beam Instabilities as Generation Mechanism of Electrostatic Solitary Waves in the Magnetotail, *J. Geophys. Res.*, **101**, 2,685–2,697, 1996.

Thorne, R. M. and B. T. Tsurutani, Resonant interactions between cometary ions and low frequency electromagnetic waves, *Planet. Space Sci.*, **35**, 1501–1511, 1987.

Ueda, H., Y. Omura, H. Matsumoto, and T. Okuzawa, A study on the numerical heating in electrostatic particle simulations, *Comput. Phys. Comm.*, **79**, 249–259, 1994.

Umeda, T., Y. Omura, T. Tominaga, and H. Matsumoto, A new charge conservation method in electromagnetic particle-in-cell simulations, *Comput. Phys. Comm.*, **156**, 73–85, 2003.

Villasenor, J. and O. Buneman, Rigorous charge conservation for local electromagnetic field solvers, *Comput. Phys. Comm.*, **69**, 306–316, 1992.